Tidal Conversion at a Submarine Ridge

FRANÇOIS PÉTRÉLIS

Laboratoire de Physique Statistique, Ecole Normale Supérieure, Paris, France

STEFAN LLEWELLYN SMITH

Department of Mechanical & Aerospace Engineering, Jacobs School of Engineering, University of California, San Diego, La Jolla, California

W. R. YOUNG

Scripps Institution of Oceanography, University of California, San Diego, La Jolla, California

(Manuscript received 30 July 2003, in final form 20 January 2004)

ABSTRACT

The radiative flux of internal wave energy (the "tidal conversion") powered by the oscillating flow of a uniformly stratified fluid over a two-dimensional submarine ridge is computed using an integral-equation method. The problem is characterized by two nondimensional parameters, A and B. The first parameter, A, is the ridge half-width scaled by μh, where h is the uniform depth of the ocean far from the ridge and μ is the inverse slope of internal tidal rays (horizontal run over vertical rise). The second parameter, B, is the ridge height scaled by h. Two topographic profiles are considered: a triangular or tent-shaped ridge and a "polynomial" ridge with continuous topographic slope. For both profiles, complete coverage of the (A, B) parameter space is obtained by reducing the problem to an integral equation, which is then discretized and solved numerically. It is shown that in the supercritical regime (ray slopes steeper than topographic slopes) the radiated power increases monotonically with B and decreases monotonically with A. In the subcritical regime the radiated power has a complicated and nonmonotonic dependence on these parameters. As $A \to 0$ recent results are recovered for the tidal conversion produced by a knife-edge barrier. It is shown analytically that the $A \to 0$ limit is regular: if $A \ll 1$ the reduction in tidal conversion below that at $A = 0$ is proportional to A^2. Further, the knife-edge model is shown to be indicative of both conversion rates and the structure of the radiated wave field over a broad region of the supercritical parameter space. As A increases the topographic slopes become gentler, and at a certain value of A the ridge becomes "critical"; that is, there is a single point on the flanks at which the topographic slope is equal to the slope of an internal tidal beam. The conversion decreases continuously as A increases through this transition. Visualization of the disturbed buoyancy field shows prominent singular lines (tidal beams). In the case of a triangular ridge these beams originate at the crest of the triangle. In the case of a supercritical polynomial ridge, the beams originate at the shallowest point on the flank at which the topographic slope equals the ray slope.

1. Introduction

The passage of the barotropic tide over submarine topography is a main source of the mechanical energy required to power the internal gravity wave field and mix the stably stratified ocean (Ledwell et al. 2000; Munk and Wunsch 1998). Satellite altimetry has shown deep-sea tidal energy losses concentrated at submarine ridges and island arcs (Egbert and Ray 2001; Ray and Mitchum 1996). Observational and modeling studies have focused on the Hawaiian Ridge as an accessible site at which these processes might be investigated (Merrifield and Holloway 2002; Rudnick et al. 2003). Thus, there is a powerful motivation to understand the factors that control the tidally powered radiation of internal gravity waves (the "tidal conversion") from a realistically steep and tall ridge.

Corresponding author address: W. R. Young, Scripps Institution of Oceanography, University of California, San Diego, La Jolla, CA 92023-0230.
E-mail: wryoung@ucsd.edu

The main theoretical approach to this tidal conversion problem uses ideas developed first by Bell (1975a,b; see also Khatiwala 2003; Llewellyn Smith and Young 2002; St. Laurent and Garrett 2002). In Bell's work the crucial approximations are that topographic slopes are small relative to the slope of internal tidal beams, and that the height of the topography is much less than the depth of the ocean. With these two restrictions, the bottom boundary condition can be applied approximately at a flat surface, say $z = 0$. This simplification allows the linear superposition of different topographic sinusoids and the application of Fourier analysis so that the conversion rate is obtained in terms of the topographic spectral density. We refer to the two approximations introduced by Bell as the weak topography approximation (WTA).

Independent of Bell, in 1973 P. G. Baines developed a procedure that avoids linearization of the bottom boundary condition around $z = 0$. At first, Baines also restricted consideration to the subcritical case, in which the slope of the topography is everywhere less than the slope of the tidal beams (referred to by Baines as "flat bump" topography). In 1982, Baines dealt with the complementary case of supercritical topography ("steep" topography). Thus, using the method of Baines (1973, 1982) one can, in principle, deal with arbitrary topography, but the calculations are difficult, particularly for the supercritical case, where Baines was forced to make some additional approximations. In this article we will develop a fresh approach to the problem of tidal generation by a submarine ridge. Our method, based on results of Robinson (1969) and Llewellyn Smith and Young (2003), works in both the sub- and supercritical cases and results in compact estimates of the radiated tidal energy.

We consider several idealized models of a submarine ridge (see Fig. 1) and attempt a broad survey of parameter space. But we also have in mind the specific example of the Hawaiian Ridge. The height of the Hawaiian Ridge is comparable to the depth of the ocean, and the slope of the flanks is significantly steeper than the slope of internal wave rays (i.e., the Hawaiian Ridge is strongly supercritical). For both these reasons, the WTA is inapplicable to Hawaii. The most relevant Hawaiian example from the work of Baines is the "symmetric cosine ridge" (Baines 1973). However, Baines's results for the symmetric cosine are restricted to the subcritical case.

Recent work by St. Laurent et al. (2003) provides the first theory that comes to grips with the strongly supercritical topography characteristic of Hawaii. Two relevant topographic profiles from St. Laurent et al. are the "knife-edge barrier" and the "top-hat ridge." In the case of the knife edge, a two-dimensional ridge of width $-a < x < a$ and height $0 < z < b$ is replaced by a knife edge (zero width) of the same height, b. The knife edge is the most extreme example of a strongly supercritical ridge and can be regarded as the end member of a family of topographic profiles in which $a \to 0$ with b fixed. This knife-edge model is particularly useful because it can be solved analytically (Llewellyn Smith and Young 2003). St. Laurent et al.'s solution of the top-hat ridge shows that broadening the knife into a flat-topped block makes only a small increase in the conversion rate above that of a knife edge with the same height. This anticipates one of our results based on the profiles in Fig. 1: the seemingly pathological knife edge provides quantitatively accurate estimates of the conversion produced by strongly supercritical ridges of finite width. Moreover, aside from interesting details close to the ridge, the radiation pattern of the knife edge is very similar to that of finite-width ridges (see Fig. 1). A limi-

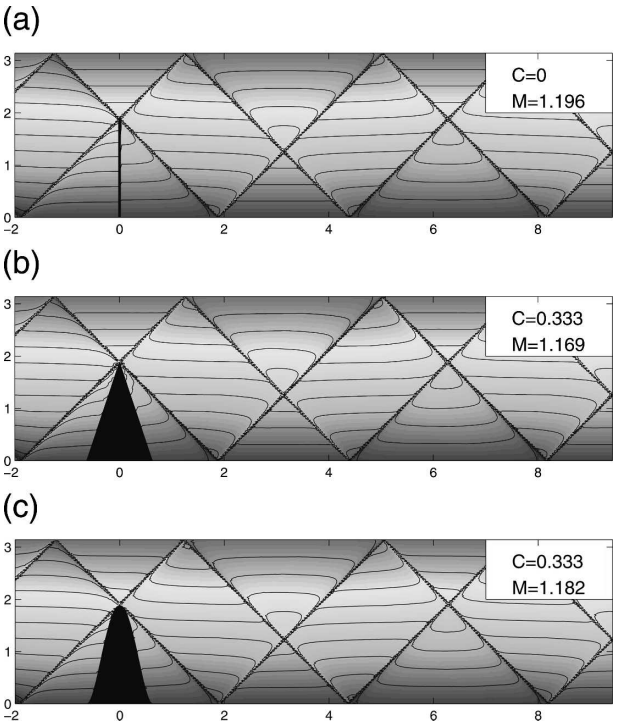

FIG. 1. Snapshots of the total buoyancy field, $N^2z + \theta$ in (2.8), associated with the internal tide radiation from three idealized supercritical ridges, all with $b/h = 3/5$. (top) The knife-edge ridge with $C \equiv a/\mu b = 0$. (middle) The triangular ridge in (2.1) with $C \equiv a/\mu b = 1/3$. (bottom) The "polynomial" ridge in (2.2) with $C \equiv a/\mu b = 1/3$. This figure uses nondimensional coordinates in which the depth of the ocean is $0 < Z < \pi$ and tidal rays travel at 45° paths. The tidal beams are the prominent linear singularities originating at, or near, the ridge crest. The nondimensional conversion factor M, defined in (1.3), varies by less than 7% among the three different cases.

tation of the abrupt topographies analyzed by St. Laurent et al. (2003) is that one cannot study the transition from sub- to supercritical topography by continuously varying the slope of the ridge flanks. This is a motivation for studying the profiles in the lower panels of Fig. 1: with fixed height one can start in the knife-edge limit and smoothly increase the width of the ridge. During this process the slope of the flanks decreases monotonically and continuously, and at a particular width the ridge becomes completely subcritical; that is, the topographic slopes are everywhere less than the ray slopes of internal gravity waves. Thus, the super- to subcritical transition is captured. Provided that the ridge height is much less than the ocean depth, further increases in the width move one into the domain of validity of the WTA.

We focus exclusively on the two-dimensional problem and represent the tidal flow as

$$\mathbf{U} = U\cos(\omega t)\hat{\mathbf{x}}, \tag{1.1}$$

where $\hat{\mathbf{x}}$ is a unit vector in the x direction. This oscillatory flow impinges on a ridge of height b and width $2a$. The ocean has total depth h so that the gap above the ridge crest is $h - b$ (see Fig. 2). In addition to the tidal frequency ω there are two other important frequencies in this problem: the Coriolis frequency f and the buoyancy frequency N (assumed to be uniform). From these three frequencies, and the internal wave dispersion relation, we obtain the inverse slope (run over rise) of internal tidal rays in terms of the dimensional parameter[1]:

$$\mu \equiv \frac{N}{\sqrt{\omega^2 - f^2}}. \tag{1.2}$$

Consider parameters roughly matching Hawaii: $f = 5 \times 10^{-5}\ \mathrm{s}^{-1}$ and $\omega = 2.8f$ (corresponding to a 12.4-h tidal period). For the buoyancy frequency we use the vertical average of N near Hawaii, estimated by Llewellyn Smith and Young (2003) as close to one cycle per hour, or $N = 35f$. With these numbers, $\mu \approx 13.5$. Thus a tidal beam rises vertically through 1 m for every 13.5 m of horizontal excursion. Realistic topographic slopes can easily be steeper than one part in 13.5. One of our conclusions is that in both the sub- and supercritical cases the converted tidal power is best written in terms of the external dimensional variables as

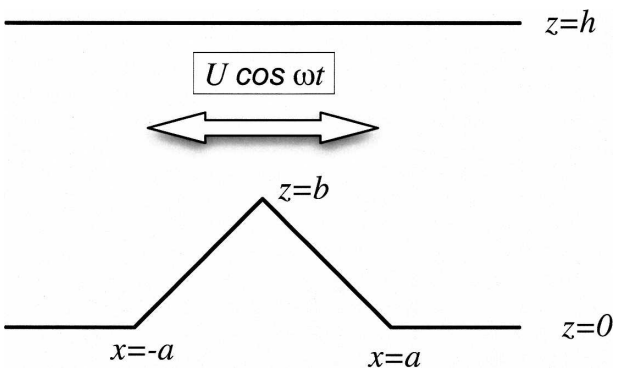

FIG. 2. Geometry of the triangular ridge. The height of the ridge is b, and the width at the base is $2a$; the total depth of the ocean is h. The nondimensional inverse slope is $C \equiv a/\mu h$, where μ is the inverse slope of internal tidal rays given in (1.2).

$$C = \frac{\pi}{4} b^2 \rho U^2 N \sqrt{1 - \frac{f^2}{\omega^2}} \times M\left(\frac{b}{h}, \frac{a}{\mu h}, \frac{\omega}{N}, \frac{U}{\omega a}, \cdots\right), \tag{1.3}$$

where ρ is the average density of seawater and M is a dimensionless function. The dimensions of C are watts per meter of ridge. The expression in (1.3) is constructed so that the strongest dependence of C on the external parameters is contained in the dimensional prefactor.

As a numerical example, take $b = 4500$ m, $\rho = 1000$ kg m^{-3}, and $U = 0.01$ m s^{-1}. For the frequencies we use values of (ω, N, f) in the previous paragraph. Then the dimensional prefactor in (1.3) is

$$\frac{\pi}{4} b^2 \rho U^2 N \sqrt{1 - \frac{f^2}{\omega^2}} \approx 2.6 \times 10^3\ (\mathrm{W\ m^{-1}}). \tag{1.4}$$

If the length of the ridge is 2000 km then the total conversion is $5.2 \times M$ GW. Llewellyn Smith and Young (2003) showed that in a realistically stratified ocean, with N being a strong function of z, a more accurate estimate is obtained by using N evaluated at the ridge crest, $z = b$, in formulas such as (1.3). If the ridge penetrates the thermocline this can easily increase (1.4) by a factor of 2 or 3.

It is interesting to compare (1.4) with observational estimates of energy flux. Near the Hawaiian Ridge estimated fluxes are in the range 6 to 15×10^3 W m^{-1} (Ray and Mitchum 1996; Kang et al. 2000; Egbert and Ray 2001; Merrifield et al. 2001; Merrifield and Holloway 2002). For the Mendocino Escarpment, a recent

[1] Because $N \gg \omega$ the hydrostatic approximation is formally justified. We make this simplification in (1.2) and throughout the paper. However, $N \gg \omega$ does not ensure that the hydrostatic approximation is uniformly valid: the radiated wave field develops very small length scales within the internal tidal beams. These singularities result in density inversions and localized failure of both the hydrostatic approximation and the linearization assumption (see section 6).

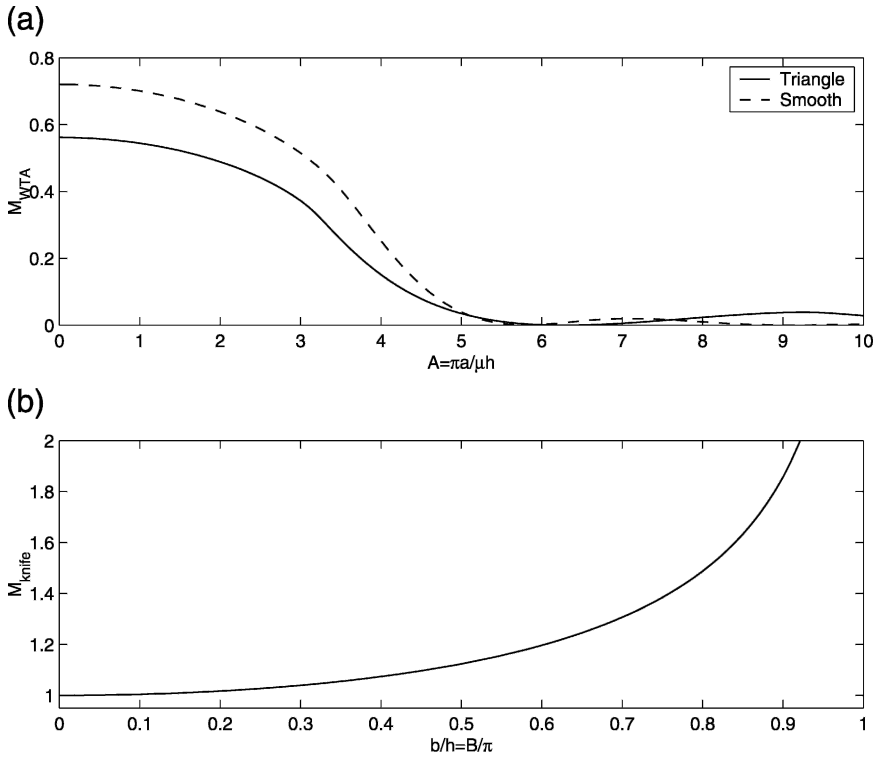

FIG. 3. (top) The function $M_{\mathrm{WTA}}(A)$ defined by the right-hand sides of (2.6) and (2.7) for triangular and polynomial ridges, respectively. Note that $\lim_{A\to 0} M_{\mathrm{WTA}}(A) = 8\ln 2/\pi^2 \approx 0.562$ for the triangle and $64/9\pi^2 \approx 0.721$ for the polynomial ridge. (bottom) The function $M_{\mathrm{knife}}(B)$ defined by the right-hand side of (1.7).

estimate is 7×10^3 W m^{-1} (Althaus et al. 2003). For the Aleutian Ridge, Cummins et al. (2001) estimate a flux of 3×10^3 W m^{-1}.

In (1.3), C depends quadratically on the height of the ridge through the factor b^2. This quadratic dependence on the ridge height b is apparent in Baines's (1973) results for the subcritical symmetric cosine ridge (see his Fig. 6). There is some weaker residual dependence on b contained in the function M. Moreover, the strongest dependence of M on the various nondimensional groups is through the first two: b/h and $a/\mu h$. The successive arguments, ω/N, $U/(\omega a)$, and so on, are all small parameters. For brevity we will suppress reference to these small parameters and regard M mainly as a function of the nondimensional ridge height b/h and the nondimensional half-width $a/\mu h$.

Thus, one of our main goals is to understand quantitatively the tidal conversion produced by the idealized ridges of Fig. 1 by calculating the function $M(b/h, a/\mu h)$. There are two limiting cases already understood from earlier investigations. The first case is the WTA, obtained from the limit

$$M_{\mathrm{WTA}}\left(\frac{a}{\mu h}\right) = \lim_{b/h\to 0} M\left(\frac{b}{h}, \frac{a}{\mu h}\right). \tag{1.5}$$

The upper panel of Fig. 3 shows the functions $M_{\mathrm{WTA}}(a/\mu h)$ corresponding to the triangular and the polynomial topographic profiles in the lower panels of Fig. 1. These results are obtained using the formulas in either Khatiwala (2003) or Llewellyn Smith and Young (2002) [see (2.6) and (2.7) below].

The second analytic case is that of a knife-edge barrier, corresponding to

$$M_{\mathrm{knife}}\left(\frac{b}{h}\right) = \lim_{a/\mu h\to 0} M\left(\frac{b}{h}, \frac{a}{\mu h}\right) \tag{1.6}$$

(St. Laurent et al. 2003). In this instance, Llewellyn Smith and Young (2003) have shown that

$$M_{\mathrm{knife}}\left(\frac{b}{h}\right) = \frac{4}{\pi B^2}\int_0^B Z\sqrt{\frac{1-\cos Z}{\cos Z - \cos B}}\,dZ, \tag{1.7}$$

where $B \equiv \pi b/h$ is the nondimensional height of the ridge. The right-hand side of (1.7) is shown in the lower panel of Fig. 3. Notice that M is defined so that $M_{\mathrm{knife}}(0) = 1$ and $M_{\mathrm{knife}}(b/h)$ increases monotonically with b/h. However, the rise is gradual and it is not until $b/h = 0.92$ that M_{knife} reaches 2. Again, this emphasizes

that the main dependence of C on the ridge height b is through the factor b^2 on the right-hand side of (1.3).

The domain of validity of the approximation M_{WTA} has no overlap with that of M_{knife}. Indeed, Fig. 3 shows that the limits in (1.5) and (1.6) do not commute. This is obvious physically: taking first $a/\mu h \to 0$ we bid adieu forever to the WTA. One of goals here is to "fill in" the parameter space between the two analytic cases, M_{WTA} and M_{knife}, shown in Fig. 3. In an earlier discussion of this issue, St. Laurent et al. (2003) emphasized that the conversion produced by a knife-edge ridge with $B \ll 1$ is just 2 times that of a witch of Agnesi ridge with the same height but a small slope. In other words, the WTA, extrapolated recklessly to $A = 0$, is in error by a factor of 2. For the triangular and polynomial ridge profiles used here, this reckless extrapolation gives $1/0.562 = 1.78$ and $1/0.721 = 1.39$, rather than 2. Thus, an annoying open issue concerns the behavior of M in the gap between the knife-edge limit and the WTA: as A increases with B fixed does M have an intermediate maximum, or does M decrease monotonically? Our results show that in the supercritical regime, M decreases monotonically as A increases with B fixed. While the form of this transition is interesting, and rather sensitive to the topographic profile, there is no intermediate maximum. In the subcritical regime, M has complicated nonmonotonic structure.

In section 2 we formulate the problem of tidal conversion by a ridge using a method originally developed by Robinson (1969). Robinson obtained an analytic expression for the Green's function, or "vortex solution," of the internal gravity wave equation. This Green's function represents waves propagating away from a point source in an ocean of finite depth h. By superposing these singular solutions along the surface of the ridge with a weight function, one can enforce the topographic boundary condition and so transform the problem into an integral equation. The solution of this integral equation is the weight function. For the knife problem this was the approach taken by Llewellyn Smith and Young (2003). In that case the integral equation was solved analytically and resulted ultimately in (1.7). In the present problem, with nonzero half-width, a, the integral equation is more complex, and a numerical solution in section 3 is our main approach. Results are presented in section 4. In section 5, we investigate the limit of a narrow ridge with an arbitrary profile. We show that the knife edge is obtained as a regular limit by taking the nondimensional half-width, $A \equiv \pi a/\mu h$, to zero. We present conclusions in section 6. Appendix A contains formulas and details underlying our numerical solution of the integral equation. In appendix B we investigate the limit in which the faces of the triangular ridge are almost critical, that is, the topographic slope b/a is almost equal to the ray slope μ^{-1}. This "critical" ridge presents challenges to the numerical method of section 4, so the analytic results of appendix B establish a useful landmark in the parameter space.

2. Formulation

a. The ridge

We idealize the ocean as a rotating, inviscid fluid layer in which the tide sloshes to and fro along the x direction, as in (1.1); z denotes the vertical. We assume that the ridge is symmetric about $x = 0$. We use two main models of the submarine topography: the triangular ridge

$$z = \begin{cases} b(1 - |x|/a), & \text{if } |x| \le a, \\ 0, & \text{otherwise,} \end{cases} \tag{2.1}$$

and a "polynomial ridge"

$$z = \begin{cases} b[1 - (x/a)^2]^2, & \text{if } |x| \le a, \\ 0, & \text{otherwise.} \end{cases} \tag{2.2}$$

The geometry of the triangular ridge is illustrated in Fig. 2. In both cases the maximum height of the topography is b and the ridge width at the base is $2a$. For subsequent developments it is convenient to write the bottom boundary in the form

$$x = \pm q(z), \tag{2.3}$$

where the function $q(z)$ decreases monotonically with increasing z, from $q(0) = a$ to $q(b) = 0$. For the triangular ridge in (2.1),

$$q(z) = a\left(1 - \frac{z}{b}\right), \tag{2.4}$$

and for the polynomial hump in (2.2),

$$q(z) = a\sqrt{1 - \sqrt{\frac{z}{b}}}. \tag{2.5}$$

We record here some results obtained by applying the WTA to the idealized ridges in (2.1) and (2.2). This approximation is valid if both $b/h \ll 1$ and $\mu b/a \ll 1$. Then the formulas in either Khatiwala (2003) or Llewellyn Smith and Young (2002), applied to the triangular ridge, give

$$M_{\mathrm{WTA}}\left(\frac{a}{\mu h}\right) = \frac{32}{\pi^2 A^2}\sum_{n=1}^{\infty} n^{-3}\sin^4\left(\frac{nA}{2}\right), \tag{2.6}$$

where $A \equiv \pi a/\mu h$ is a nondimensional half-width of the ridge. The right-hand side of (2.6) is the solid curve in the upper panel of Fig. 3. Figure 3 also shows the con-

version in the WTA limit for polynomial ridge in (2.2). In this case

$$M_{\mathrm{WTA}}\left(\frac{a}{\mu h}\right) = \frac{512}{\pi^2 A^8}\sum_{n=1}^{\infty} n^{-9}[(n^2A^2 - 3)\sin nA + 3nA\cos nA]^2. \tag{2.7}$$

For the triangular ridge, (2.6) shows that M vanishes when A is a multiple of 2π—the first of these zeroes is apparent in Fig. 3. At these special values of the ridge width there is destructive interference and no tidal conversion; no internal waves are radiated, and instead the disturbance is confined to the neighborhood of the ridge. We shall see that for the triangular ridge these "null" points survive in the general case; that is, the zeroes of M are not artifacts of the WTA. For the polynomial hump, M never exactly vanishes. But (2.7) is also very small when A is close to multiples of 2π.

b. Governing equations

The density is written as

$$\rho = \rho_0(1 - g^{-1}N^2z - g^{-1}\theta), \tag{2.8}$$

where N is the uniform buoyancy frequency and $\theta(x, z, t)$ is the buoyancy of the disturbance. Because the topography is independent of y, so too is the disturbance created by tidal action. The governing equations for the induced velocity (u, v, w), rescaled pressure p, and buoyancy θ are

$$\begin{aligned} u_t - fv + p_x &= 0,\\ v_t + fu &= 0,\\ p_z &= \theta,\\ \theta_t + N^2w &= 0, \quad \text{and}\\ u_x + w_z &= 0. \end{aligned} \tag{2.9}$$

In these equations f is the Coriolis frequency.

The velocity in the (x, z) plane can be represented using a streamfunction $\psi(x, z, t)$: $(u, w) = (-\psi_z, \psi_x)$. The problem then reduces to solving the internal gravity wave equation,

$$\psi_{zzt} + f^2\psi_{zz} + N^2\psi_{xx} = 0. \tag{2.10}$$

The bottom boundary condition is

$$\psi[\pm q(z), z] = Uz\cos(\omega t). \tag{2.11}$$

The condition in (2.11) ensures that the total streamfunction, $-Uz\cos(\omega t) + \psi$, vanishes on the bottom.

c. The steady-state wave field

We consider the steady-state wave conversion by looking for time-periodic solutions with the tidal frequency: we introduce $\varphi = \varphi_r + i\varphi_i$, where

$$\psi = U\Re(e^{-i\omega t}\varphi) = U(\varphi_r\cos\omega t + \varphi_i\sin\omega t). \tag{2.12}$$

The function φ satisfies the hyperbolic equation

$$N^2\varphi_{xx} = (\omega^2 - f^2)\varphi_{zz}, \tag{2.13}$$

with the boundary conditions

$$\varphi[\pm q(z), z] = z \quad \text{and} \quad \varphi(x, h) = 0. \tag{2.14}$$

The mathematical problem is completed by insisting that the energy flux is away from the ridge. This radiation condition ensures that φ has both a real and an imaginary part.

Because the ridge is symmetric about $x = 0$, the solution $\psi(x, z, t)$ reverses sign every half period: $\psi(x, z, t + \pi/\omega) = -\psi(-x, z, t)$. This symmetry implies that the solution of (2.13) and (2.14) is an even function of x:

$$\varphi(x, z) = \varphi(-x, z). \tag{2.15}$$

The main quantity of interest is the conversion rate of barotropic tidal energy into internal gravity waves. To calculate the conversion rate we begin with the energy equation obtained from (2.9):

$$\frac{1}{2}(u^2 + v^2 + N^{-2}\theta^2)_t + \psi_x p_z - \psi_z p_x = 0. \tag{2.16}$$

For the periodic flow, the average of (2.16) over the tidal cycle implies that

$$\nabla\cdot\mathbf{J} = 0, \tag{2.17}$$

where $\mathbf{J}$ is the phase average of the energy flux $(\psi p_z, -\psi p_x)$; using (2.12) this phase-averaged flux can be written as

$$\mathbf{J} = \frac{iU^2\rho_0}{4\omega}[N^2(\varphi\varphi_x^* - \varphi^*\varphi_x),\ -(\omega^2 - f^2)(\varphi\varphi_z^* - \varphi^*\varphi_z)]. \tag{2.18}$$

d. The Green's function

The main tool used in this work is Green's function $\mathcal{G}(x - x', z, z')$, found by Robinson (1969). This fundamental function is defined by

$$N^2\mathcal{G}_{xx} - (\omega^2 - f^2)\mathcal{G}_{zz} = (iN^2/\mu)\delta(x - x')\delta(z - z'), \tag{2.19}$$

with the boundary conditions that

$$\mathcal{G}(x - x', 0, z') = \mathcal{G}(x - x', h, z') = 0. \tag{2.20}$$

The definition of $\mathcal{G}$ is completed by requiring that there is only outgoing radiation. Explicitly, this Green's function is

$$\mathcal{G}(x - x', z, z') = \frac{1}{\pi}\sum_{n=1}^{\infty} n^{-1} \sin nZ \sin nZ' e^{in|X-X'|}, \tag{2.21}$$

where (X, Z) are nondimensional coordinates defined by

$$X \equiv \frac{\pi x}{\mu h} \quad \text{and} \quad Z \equiv \frac{\pi z}{h}. \tag{2.22}$$

Notice that the nondimensional depth of the ocean is π and that tidal beams travel at 45° in the (X, Z) plane.

e. The integral equation

Using the Green's function $\mathcal{G}$ we represent the solution of (2.13) as a linear superposition of singularities located on both the positive and negative sides of the ridge. If the density of singularities is $\gamma(z)$ then the representation is

$$\varphi(x, z) = \frac{1}{2}\int_0^b \gamma(z')\{\mathcal{G}[x + q(z'), z, z'] + \mathcal{G}[x - q(z'), z, z']\}\, dz'. \tag{2.23}$$

Notice that to enforce the symmetry (2.15) we have used the same density, $\gamma(z)$, on both $x = \pm q(z)$. [For an asymmetric ridge one would use different densities $\gamma_{\pm}(z)$ on $x = q_{\pm}(z)$.]

Evaluating (2.23) on the topography, $x = \pm q(z)$, produces our integral equation

$$z = \int_0^b \gamma(z')\mathcal{R}(z, z')\, dz'. \tag{2.24}$$

Using the notation $q' \equiv q(z')$, the kernel is

$$\mathcal{R}(z, z') = \frac{1}{2}\mathcal{G}(q + q', z, z') + \frac{1}{2}\mathcal{G}(q - q', z, z'), \tag{2.25}$$

where $\mathcal{G}$ is the Green's function in (2.21). If $q = q' = 0$ this integral equation collapses to that solved by Llewellyn Smith and Young (2003).

The kernel $\mathcal{R}$ is a complex function with the symmetry $\mathcal{R}(z, z') = \mathcal{R}(z', z)$. An explicit expression for $\mathcal{R}$ based on the series in (2.21) is

$$\mathcal{R}(z, z') = \frac{1}{2\pi}\sum_{n=1}^{\infty} n^{-1} \sin nZ \sin nZ' [e^{in(Q+Q')} + e^{in|Q-Q'|}], \tag{2.26}$$

where $Q(Z) \equiv \pi q(z)/\mu h$ is the nondimensional bottom function.

For the models in (2.4) and (2.5) the nondimensional bottom functions are

$$Q(Z) = A\left(1 - \frac{Z}{B}\right) \quad \text{and} \quad Q(Z) = A\sqrt{1 - \sqrt{\frac{Z}{B}}}, \tag{2.27}$$

where $A = \pi a/\mu h$ and $B = -\pi z/h$.

f. Energy flux and conversion

We obtain the conversion, C in (1.3), most simply by calculating the total outgoing energy flux at a large distance from the ridge:

$$C = 2\int_0^h \mathbf{J}(x \geq a, z) \cdot \hat{\mathbf{x}}\, dz, \tag{2.28}$$

where $\mathbf{J}$ is the flux in (2.18), and the factor of 2 on the right-hand side accounts for the energy radiated to $x < 0$.

If x is positive and large (the far field) then the representation in (2.23) condenses to

$$\varphi(x, z) = \frac{h}{\pi}\sum_{n=1}^{\infty} \frac{\gamma_n}{n} \sin nZ\, e^{inX}, \tag{2.29}$$

where

$$\gamma_n \equiv \frac{1}{\pi}\int_0^B \gamma(Z') \sin nZ' \cos[nQ(Z')]\, dZ'. \tag{2.30}$$

Inserting (2.30) into (2.28) gives

$$C = \frac{1}{2\pi}\rho U^2 h^2 \sqrt{1 - \frac{f^2}{\omega^2}} N \sum_{n=1}^{\infty} \frac{\gamma_n \gamma_n^*}{n}. \tag{2.31}$$

The function M defined by (1.3) is then

$$M = \frac{2}{B^2}\sum_{n=1}^{\infty} \frac{\gamma_n \gamma_n^*}{n}. \tag{2.32}$$

Substituting (2.30) into (2.32) and exchanging summation with integration gives

$$M = \frac{2}{\pi B^2}\int_0^B dZ \int_0^B dZ' \gamma(Z)\gamma^*(Z')\mathcal{R}_r(Z, Z'), \tag{2.33}$$

where $\mathcal{R}_r(Z, Z')$ is the real part of $\mathcal{R}(Z, Z')$ in (2.26). Using the integral equation in (2.24) and the symmetry $\mathcal{R}(Z, Z') = \mathcal{R}(Z', Z)$, we can eliminate the double integral in (2.33) and show that

$$M = \frac{2}{\pi B^2} \int_0^B \gamma_r(Z) Z \, dZ, \tag{2.34}$$

where $\gamma_r(Z)$ is the real part of $\gamma(Z)$. In (2.32), (2.33), and (2.34) we now have three different expressions for the function M defined in (1.3). We will use each of these representations for different purposes in the sequel.

3. Solving the integral equation

The integral equation in (2.24), rewritten in terms of nondimensional variables, is

$$Z = \int_0^B \mathcal{R}(Z, Z')\gamma(Z') \, dZ', \tag{3.1}$$

where the kernel $\mathcal{R}$ is defined by the series in (2.26). This is a Fredholm integral equation of the first kind.

We discretize the coordinate $0 < Z < B$ using a grid Z_n, $n = 0, 1, \ldots, N$. We used both the "Chebyshev grid," $Z_n = B \sin(\pi n/2N)$, and the "squared Chebyshev grid," $Z_n = B \sin^2(\pi n/2N)$. Both grids increase resolution near the crest of the ridge. The second also increases resolution near the base of the ridge. The midpoint of the nth interval is $\overline{Z}_n \equiv (Z_n + Z_{n-1})/2$, and the grid spacing is $\Delta_n \equiv Z_n - Z_{n-1}$. In interval n, where $Z_{n-1} < Z < Z_n$, we represent the topography as

$$Q(Z) = \tilde{Q}_n - S_n Z, \tag{3.2}$$

where

$$\tilde{Q}_n = \frac{Z_n Q_{n-1} - Z_{n-1} Q_n}{Z_n - Z_{n-1}}, \tag{3.3}$$

with $Q_n \equiv Q(Z_n)$ and $S_n \equiv -(Q_n - Q_{n-1})/\Delta_n$. Since $Q(Z)$ is monotonically decreasing, our definition ensures that $S_n > 0$. This positivity simplifies subsequent absolute value signs.

To ensure that the discretization maintains the symmetric structure of the kernel we integrate (3.1) from $Z = Z_{n-1}$ to $Z = Z_n$ and obtain

$$\frac{1}{2}(Z_n^2 - Z_{n-1}^2) = \int_0^B \overline{\mathcal{R}}_n(Z')\gamma(Z') \, dZ', \quad n = 1, \ldots, N, \tag{3.4}$$

where

$$\overline{\mathcal{R}}_n(Z') \equiv \int_{Z_{n-1}}^{Z_n} \mathcal{R}(Z, Z') \, dZ. \tag{3.5}$$

Next, we discretize the Z' integral in (3.4) to obtain a set of N linear equations for the unknowns $\gamma_k \equiv \gamma(\overline{Z}_k)$:

$$\frac{1}{2}(Z_n^2 - Z_{n-1}^2) = \sum_{k=1}^{N} \mathbf{W}_{nk} \gamma_k, \quad n = 1, \ldots, N, \tag{3.6}$$

where

$$\mathbf{W}_{nk} = \int_{Z_{n-1}}^{Z_n} dZ \int_{Z_{k-1}}^{Z_k} dZ' \, \mathcal{R}(Z, Z'). \tag{3.7}$$

Notice that the $N \times N$ matrix $\mathbf{W}_{nk}$ is symmetric but not Hermitian. The linear system (3.6) can be solved with standard techniques to yield γ_k, and then M is obtained from the discretized version of (2.34):

$$M = \frac{2}{\pi B^2} \sum_{k=1}^{N} \Re(\gamma_k) \overline{Z}_k \Delta_k. \tag{3.8}$$

The calculation of the matrix $\mathbf{W}_{nk}$ is detailed in appendix A. Table 1 summarizes the numerical parameters used to obtain the results in this paper.

The numerical solution of Fredholm integral equations of the first kind is not entirely straightforward. The numerical procedure described above reduces the integral equation to the matrix equation in (3.6), and the difficulty is that the matrix $\mathbf{W}_{nk}$ is sometimes ill conditioned (i.e., nearly singular). We were unprepared for this possibility because in the earlier case of the knife-edge barrier ($C = 0$) the kernel of the integral equation is so singular that (3.6) is well conditioned. Unpleasantly, this is not characteristic of the general case $C \neq 0$. Thus, while the numerical solution to (3.6) exists, it sometimes (depending on A and B) contains small-scale noise that does not disappear as the resolution N is increased. Some examples are shown in Fig. 4.

TABLE 1. Parameters used in the numerical solution of the integral equation. Here N is the number of grid points, e.g., for the Chebyshev grid $Z_n = B \sin(\pi n/2N)$. To calculate the matrix $\mathbf{W}_{nk}$ in (3.7) using the method described in appendix A we truncate the series in (A.4)–(A.7) at $p = P$. In the neighborhood of $C = 1$ for the triangle and $C = 1.5$ for the polynomial ridge, the series is slowly convergent, and we increase P as indicated above.

Figures	N	P
1, 6, 8	320	5000
4	320	300 000 for $C = 1.5$ and 20 000 for $C = 1.75$
5, 9 (top)	40	300 000 for $0.95 \leq C \leq 1.05$; 20 000 otherwise
7, 9 (bottom)	40	300 000 for $1.1 \leq C \leq 1.5$; 20 000 otherwise
11	20	20 000

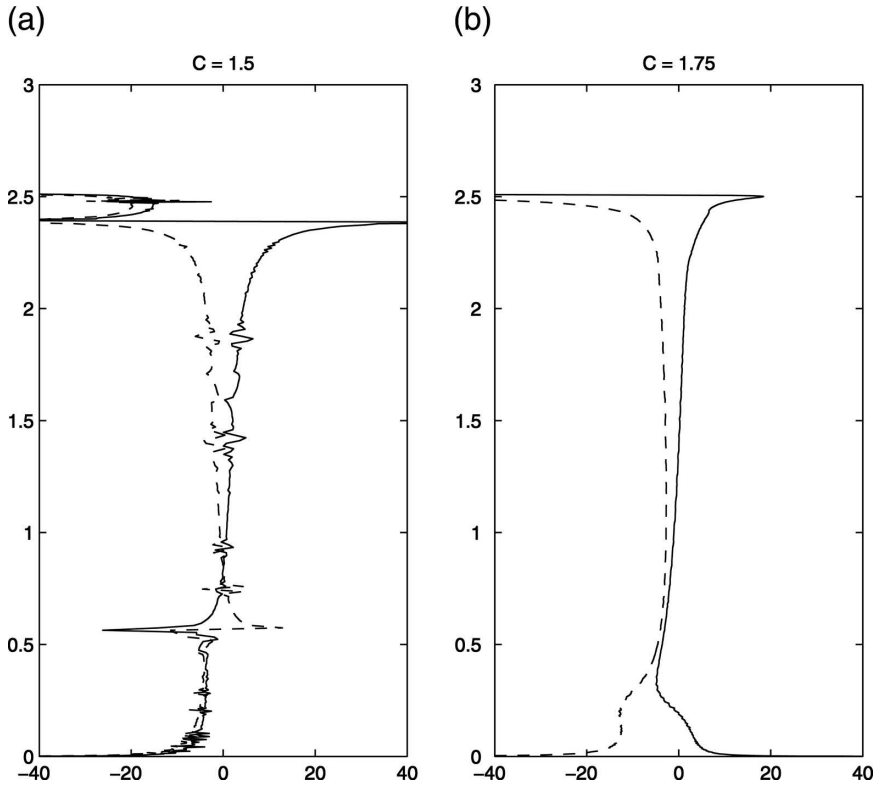

FIG. 4. Weight functions, $\gamma(Z)$, for the polynomial ridge. The vertical coordinate is $0 < Z < B = 0.8\pi$. Solid curves: real part of $\gamma(Z)$; dotted curves: imaginary part of $\gamma(Z)$. (left) A worst case; (right) a best case. The small-scale noise in the left-hand panel arises because the matrix $\mathbf{W}_{nk}$ in (3.6) is nearly singular.

However, the conversion rate is an integral of the weight function, given by the sum (3.8) in the numerical formulation. Because integration is a smoothing operation, M converges as the resolution is increased, despite the noise in γ. Similarly, the field $\varphi(x, y)$ is also an integral of the weight function, as in (2.23), and this integral is also forgiving of small-scale noise in $\gamma(z)$. Nevertheless, in plots of the buoyancy field, values of γ very close to the peak of the topography were neglected. In addition, we used a filter to smooth Gibbs's phenomena from the solution.

4. Results

The density $\gamma(z)$ is obtained by solving the integral equation in (2.24). We discretize the interval $0 \le z \le b$ using the procedure outlined in section 3. With $\gamma(z)$ in hand, the function M is most conveniently calculated using (3.8).

a. The triangular ridge

In the top panel of Fig. 5, M for the triangular ridge is plotted as a function of the variable

$$C \equiv \frac{A}{B} = \frac{a}{\mu b}, \tag{4.1}$$

where C is the ratio of the inverse ridge slope, a/b, to the inverse ray slope $\mu \equiv N/\sqrt{\omega^2 - f^2}$. At $C = 0$ we recover the limit of a knife-edge barrier. As C increases the knife opens into a triangular ridge so that if $0 < C < 1$ then the triangular ridge is supercritical. At $C = 1$ the slope of the triangular ridge is critical and if $C > 1$ the slope is subcritical.

Using the inverse slope parameter C, rather than the nondimensional half-width A, collapses the curves in the top panel of Fig. 5 in the supercritical regime $0 < C < 1$ for low values of b/h. At the critical condition, $C = 1$, the function M seems to have a break in slope but remains continuous. Once $C > 1$ the ridge is subcritical and the WTA limit of a gently sloping ridge is approached, provided C is large enough. However, for practical purposes "large enough" is simply $C > 1$: the WTA result shown in the top panel of Fig. 5 is tolerably accurate once $C > 1$. This reinforces the conclusion of Balmforth et al. (2002) that the WTA works throughout the entire subcritical regime.

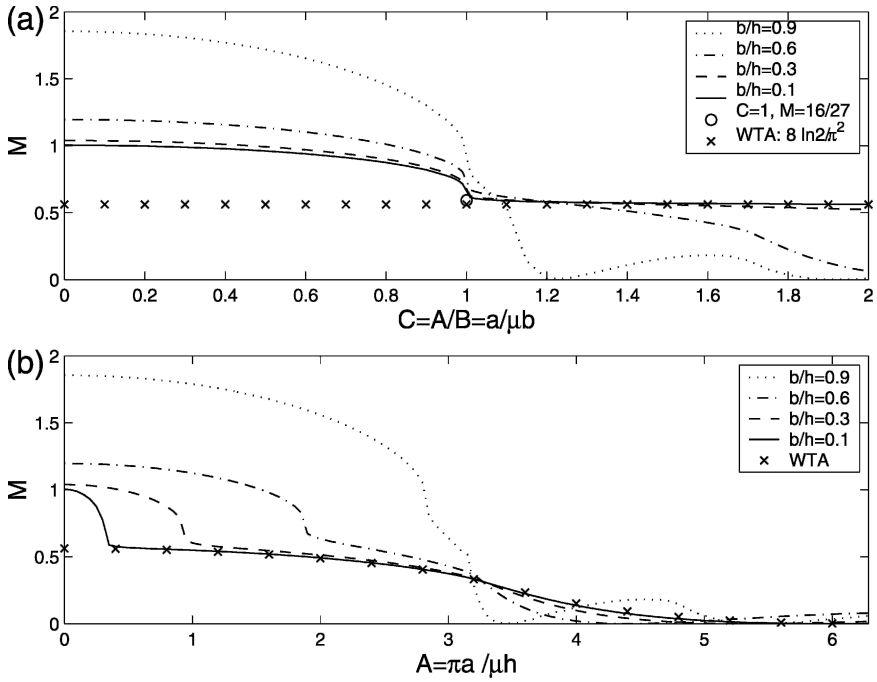

FIG. 5. (top) Function M as a function of C for the triangular ridge in (2.1). The line indicated by the times signs is the $A \to 0$ limit of the WTA series on the right-hand side of (2.6), viz., $M_{\mathrm{WTA}}(0) = 8\ln 2/\pi^2 \approx 0.562$. The open-circle point at $(1, 16/27 \approx 0.593)$ is predicted using a perturbation expansion pivoted round $b/h \ll 1$ and $C = 1$ (see appendix B). (bottom) Function M as a function of A for the triangular ridge. This presentation of the results shows the structure of the WTA approximation when A is large. With the height b/h fixed, M generally decreases as the nondimensional half-width, A, increases. However, the decrease is nonmonotonic, and the curve with $b/h = 0.9$ has a null point at which $M = 0$ (indicating no conversion) at around $A = 3.45$. For more discussion of null points see section 4d.

Also shown in the top panel Fig. 5 is the point o obtained in appendix B with an analytic reduction of (2.24) pivoted around $C \approx 1$ and $B \ll 1$. Because the numerical procedure struggles when C is close to 1, this landmark is useful as an indication of the magnitude of possible numerical errors in Fig. 5 at the critical condition. The bottom panel of Fig. 5 shows a wider view of the (A, B) parameter space. When A is greater than about 3 or 4 the function M has a rather complicated and nonmonotonic dependence on both A and B. However, in the supercritical regime, with $0 < C < 1$, the structure of M is both simple and in accord with the intuition that M increases monotonically with B and decreases monotonically with A.

The isopycnal displacements around the triangular ridge are shown in Fig. 6. Prominent disturbances forming the classic "X" of internal wave beam geometry are emitted from the crest of the triangular ridge. Much weaker disturbances also emanate from the corners at the bottom of the ridge. These faint corners in the isopycnals are visible in the $C = 0.625$ panel of Fig. 6. The panel with $C = 1.25$ shows a subcritical case. The conversion is weaker, and the secondary beams emanating from the basal corners are clear. Isopycnals between the beams are strongly distorted. The panel with $C = 1.5$ is a parameter setting at which $M = 0$; the snapshot in Fig. 6 is at an instant when there is no displacement. The panel with $C = 1.75$ shows a case in which the ridge is so wide that the main beams originating at the ridge crest reflect off the flanks before escaping.

b. The polynomial ridge

We now turn to the polynomial ridge with the profile defined in (2.2). As a nondimensional measure of the inverse slope we continue to use $C \equiv a/\mu b$ to characterize the polynomial ridge. Because the topographic slope changes continuously, the geometry of the polynomial ridge is slightly more complicated than that of the triangular ridge. The inflection points of the polynomial ridge are at

$$X = \pm A/\sqrt{3}. \tag{4.2}$$

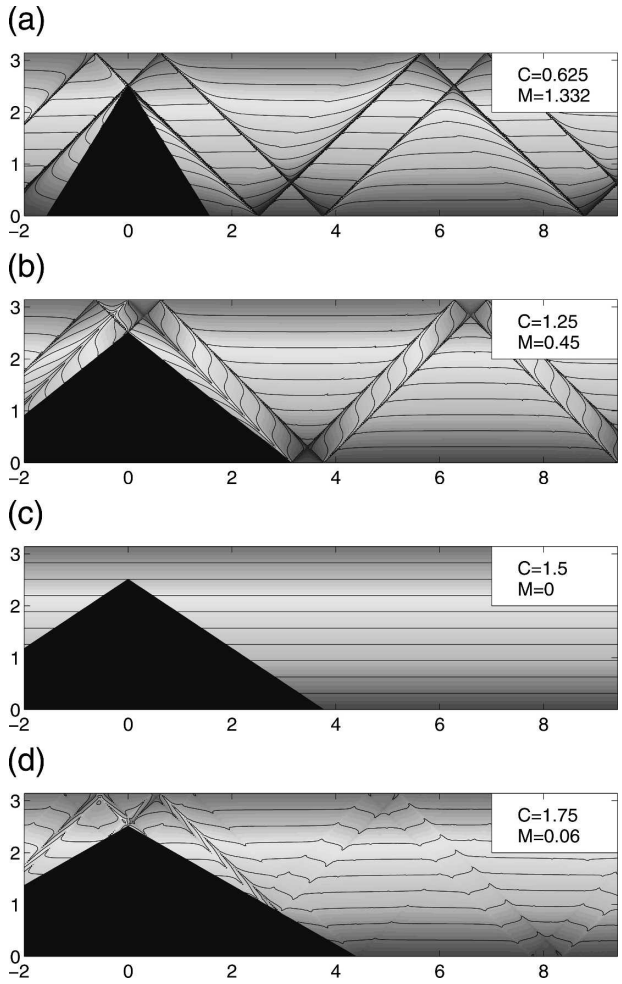

FIG. 6. Snapshots of the isopycnal patterns around a triangular ridge. In all cases $b/h = B/\pi = 0.8$. The width of the ridge is controlled by the dimensionless parameter $C = A/B = a/\mu b$; M is the dimensionless factor in (1.3). The critical condition is $C = 1$, so the top panel is supercritical and the lower three panels are subcritical. The third panel, $C = 1.5$, shows an example of a nonradiating ridge (see section 4d). Nonradiating ridges have the special property that at some phase of the tidal cycle the isopycnal disturbances vanish.

Using the nondimensional coordinates (so that the ray slope is unity) the topographic slope at these inflection points is $8/(3\sqrt{3}C)$. Because the maximum slope is at the inflection points, if $C > 8/3\sqrt{3} \approx 1.54$ then the flanks of the polynomial ridge are subcritical everywhere. On the other hand, if $C < 8/3\sqrt{3}$ then the topographic inflection points in (4.2) are surrounded by supercritical topographic slopes. The supercritical section of the flank is bounded by a both a shallow critical point and a deep critical point.

Figure 7 shows the function M in (1.3) for the polynomial ridge. The critical condition $C = 8/3\sqrt{3}$ is close to an inflection point of M as a function of the inverse slope C. However, the critical condition is not as striking as the break at $C = 1$ that is evident in Fig. 5. The lower panel of Fig. 7 shows a wider view of the (A, B) parameter space of the polynomial ridge.

Figure 8 shows snapshots of the isopycnals' displacements around the polynomial ridge. The upper three panels of Fig. 8 are all supercritical cases. In particular, the panel with $C = 1.5 < 8/3\sqrt{3}$ is slightly supercritical. The beams are emitted from the uppermost points on the ridge flank at which the topographic slope is critical. The conversion is decreasing as the beams start to merge. In the subcritical case ($C = 1.75$) the conversion is weak, as are the beams. These results are relevant to observational results such as those of Rudnick et al. (2003), who observe enhanced internal tide activity in locations above the Hawaiian Ridge and attempt to deduce its region of origin. Our results show that for the supercritical polynomial ridge the beams originate at the shallow critical points on the ridge flanks.

The top three panels of Fig. 8 illustrate some interesting differences between tidal conversion at the Hawaiian Ridge and at the Mendocino Escarpment. The Mendocino Escarpment is so steep that the internal tidal beams radiating from the crest strike the bottom without hitting the flanks on the way down (Althaus et al. 2003). The top panel of Fig. 8 shows an analogous example of a very steep ridge that is supercritical nearly all the way to the basement. Indeed, this is just the situation envisaged by the knife-edge model of St. Laurent et al. (2003). On the other hand, the simulations of conversion at Hawaii shown by Merrifield at al. (2001, 2002) show an internal tidal beam generated at the rim of the ridge crest that travels downward and reflects off the lower part of the flank where the slope is subcritical. The third panel of Fig. 8 shows this more complicated case in which the rays generated at points with supercritical slope subsequently reflect off a subcritical section of the flanks.

c. The modal split

Using the series, in (2.32) the cumulative fraction of energy flux carried by the first n modes is

$$F_n \equiv \sum_{k=1}^{n} k^{-1}\gamma_k\gamma_k^* \Big/ \sum_{k=1}^{\infty} k^{-1}\gamma_k\gamma_k^*. \tag{4.3}$$

Figure 9 shows F_1 through F_4 as a function of C at $b/h = 0.8$. At $C = 0$ (the knife), 70% of the energy is in mode 1. In both panels the fraction of energy flux in mode 1, F_1, decreases to below 0.4 as C increases to about 1.2. This result is relevant to interpreting measurements made using satellite altimetry (Ray and Mitchum 1996), which only detects mode 1. The de-

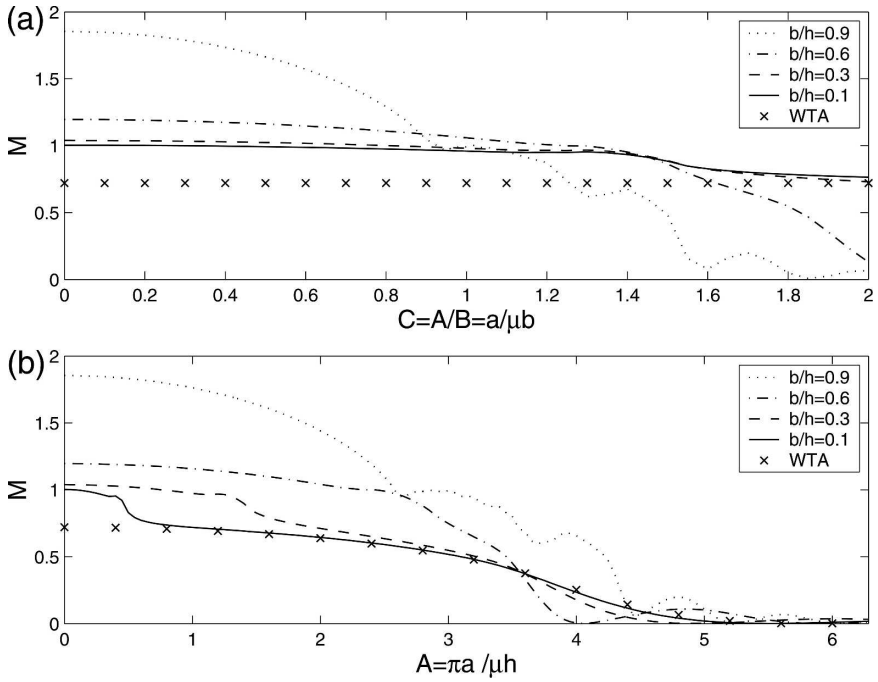

FIG. 7. (top) Function M in (1.3) as a function of the inverse slope $C = a/\mu b$ for the polynomial ridge in (2.2). The times sign denotes the $A \to 0$ limit of the WTA result in (2.7), viz., $M_{\mathrm{WTA}}(0) = 64/9\pi^2 = 0.721$. (bottom) Function M as a function of A in order to display the WTA limit.

crease in F_1 from 0.7 to below 0.4 over the range, $0 < C < 1.2$, shows that satellite altimetry could be systematically low by 50%.

d. Null points of the ridges

In the (A, B) parameter space of the triangular ridge there are "null points" at which the conversion vanishes exactly. The WTA equation in (2.6) shows that $M = 0$ at $(A, B) = (2n\pi, 0)$. Each of these points lies on a curve that extends into the (A, B) plane for nonzero B. For instance, the third panel of Fig. 6, with $C = 1.5$ and $(A, B) = (4\pi/5, 6\pi/5)$, shows another nonradiating triangular ridge with $M = 0$. Another example is the curve $b/h = 0.9$ in the lower panel of Fig. 5: that curve has a null point ($M = 0$) at around $A = 3.45$.

There is a simple geometric construction, illustrated in Fig. 10, that determines these curious nonradiating solutions of the triangular ridge. In order for the conversion to vanish, the upward ray leaving the crest, B, of the triangular ridge must reflect off the surface at S and arrive precisely at the slope break located at $X = A$ in Fig. 10. Some geometry shows that this requires

$$A + B = 2\pi. \tag{4.4}$$

This condition determines the null curve with $n = 1$. The nth null curve is determined by a ray leaving B in Fig. 10 and making n reflections at the surface before arriving at A. This geometry leads to a complicated nth order polynomial relation between A and B not presented here.

Turning now to the case of the polynomial ridge, there are also special values of A and B at which there is very little radiation: this is already apparent in the WTA equation in (2.7), which predicts very small conversion when A is a multiple of 2π. In the lower panel of Fig. 7 the dotted curve with $b/h = 0.9$ has conspicuous dips (i.e., deep minima of M) at certain values of A. These minima are polynomial-ridge analogs of the nonradiating triangular ridge. The impression one has is that when C is large rays generated near the crest of the ridge bounce off the flanks before escaping. The ensuing destructive interference is responsible for nonmonotonic dependence on ridge width in both the polynomial and triangular cases.

5. The knife-edge limit

In this section we use perturbation theory to calculate the conversion for a narrow peak that, in the limit $C \to 0$, becomes the knife-edge barrier considered by St. Laurent et al. (2003) and Llewellyn Smith and Young (2003). Although the knife-edge case has been solved exactly, this solution has been greeted with some skepticism. Clearly there is a considerable idealization involved in reducing the width of the ridge to zero while

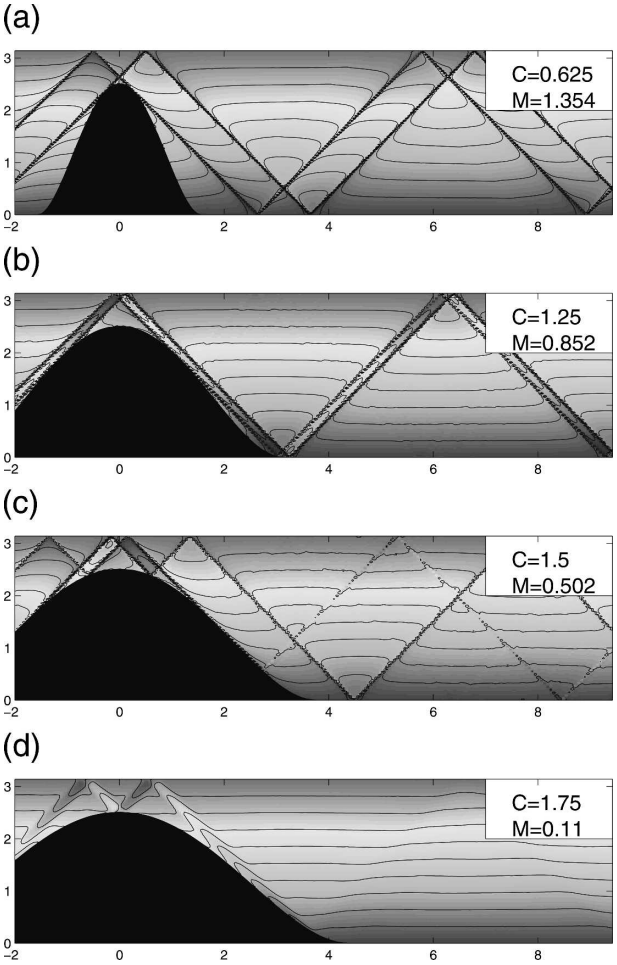

FIG. 8. Isopycnal patterns around a polynomial ridge. In all cases $b/h = B/\pi = 0.8$. The width of the ridge is controlled by the dimensionless parameter $C = A/B = a/\mu b$; M is the dimensionless factor in (1.3). The critical condition is $C = 8/[2(3)^{1/2}] \approx 1.54$; thus the upper three panels are supercritical and the bottom panel is subcritical.

fixing the height. The narrow-peak expansion in this section shows that this limit is not singular and moreover provides compact expressions for the first corrections to the results of St. Laurent et al. (2003) and Llewellyn Smith and Young (2003). We find that the knife edge is a good approximation to a ridge of finite half-width, a, provided that $a \ll \mu b$, that is, provided that the flanks of the ridge slope more steeply than the internal wave rays. In physical terms, this condition ensures that downward-traveling internal waves, generated at or near the crest of the ridge, stay well clear of the flanks.

To take the limit $a \to 0$ with b fixed we write the nondimensional topography function as $Q(z) = CQ_1(Z)$ and take $C \to 0$. The numerical results of the previous section strongly suggest that in this limit the conversion function can be expanded as a power series in C^2:

$$M = M_{\text{knife}}(B) + C^2 M_2(B) + O(C^4), \tag{5.1}$$

where $M_{\text{knife}}(B)$ is the defined on the right-hand side of (1.7) and $M_2(B)$ is a negative definite function of the ridge height, B. The numerical solution gives no indication of singular terms involving, for instance, $|C|$ or $\ln|C|$.

Our goal is to confirm the regular perturbation expansion (5.1) by explicitly calculating M_2 for the triangular profile, $Q_1(Z) = B - Z$, and for the polynomial ridge $Q_1(Z) = B\sqrt{1 - \sqrt{Z/B}}$. We proceed by solving (2.24) perturbatively with $C \ll 1$. We expand the kernel as

$$\mathcal{R}(Z, Z') = \mathcal{R}_0(Z, Z') + iC\mathcal{R}_1(Z, Z') + C^2\mathcal{R}_2(Z, Z') + O(C^3), \tag{5.2}$$

where $\mathcal{R}_n$ is obtained formally from (2.26):

$$\mathcal{R}_0(Z, Z') = \frac{1}{2\pi}\log\left|\sin\left(\frac{Z + Z'}{2}\right)\Big/\sin\left(\frac{Z - Z'}{2}\right)\right|, \tag{5.3}$$

$$\mathcal{R}_1(Z, Z') = \frac{1}{2}Q_1(Z)\delta(Z - Z'), \quad \text{and} \tag{5.4}$$

$$\mathcal{R}_2(Z, Z') = -\frac{1}{2\pi}[Q_1^2(Z) + Q_1^2(Z')] \times \sum_{n=1}^{\infty} n\sin(nZ)\sin(nZ'), \tag{5.5}$$

where $\mathcal{R}_0$ is the kernel for the knife case and both $\mathcal{R}_1$ and $\mathcal{R}_2$ are distributions. Note that these kernels are real and symmetric. The density is also expanded as $\gamma(z) = \gamma_0(z) + iC\gamma_1(z) + C^2\gamma_2(z) + O(C^3)$, where each γ_n is real.

Introducing the expansions above into the integral equation and collecting powers of C we obtain the hierarchy

$$\int_0^B \mathcal{R}_0(Z, Z')\gamma_0(Z')\,dZ' = Z, \tag{5.6}$$

$$\int_0^B \mathcal{R}_0(Z, Z')\gamma_1(Z')\,dZ' = -\int_0^B \mathcal{R}_1(Z, Z')\gamma_0(Z')\,dZ', \tag{5.7}$$

and

$$\int_0^B \mathcal{R}_0(Z, Z')\gamma_2(Z')\,dZ' = \int_0^B \mathcal{R}_1(Z, Z')\gamma_1(Z')\,dZ' - \int_0^B \mathcal{R}_2(Z, Z')\gamma_0(Z')\,dZ'. \tag{5.8}$$

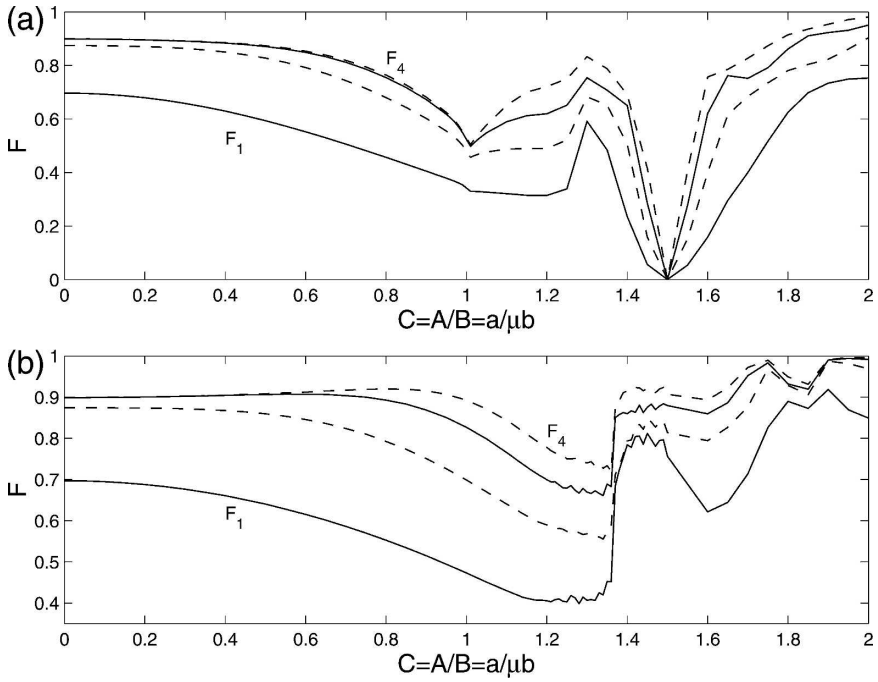

FIG. 9. (top) Fractions F_1 through F_4 for the triangular ridge as a function of C. (bottom) Fractions F_1 through F_4 for the polynomial ridge. In both cases $b/h = 0.8$. Note the different vertical scales in the two panels. The triangular ridge (top) has $M = 0$ at $C = 1.5$. Near this null point, the energy flux is no longer carried dominantly by the lowest modes.

The first equation, (5.6), was solved for $\gamma_0(z)$ by Llewellyn Smith and Young (2003):

$$\gamma_0(Z) = 2\sqrt{\frac{1-\cos Z}{\cos Z - \cos B}}. \tag{5.9}$$

At first glance it seems that we need to solve the two equations in (5.7) and (5.8) in order to use either (2.33) or (2.34) to obtain M_2. Fortunately there are some remarkable simplifications that make the calculation of M_2 rather straightforward: manipulating (but not solving) (5.6)–(5.8) we obtain

$$M_2 = \frac{1}{\pi B^2}\int_0^B Q_1(Z)\gamma_0(Z)\gamma_1(Z)\,dZ - \frac{2}{\pi B^2}\int_0^B dZ\int_0^B dZ'\,\gamma_0(Z)\gamma_0(Z')\mathcal{R}_2(Z,Z'). \tag{5.10}$$

With (5.10) we do not need to explicitly calculate $\gamma_2(z)$.

Key results leading to (5.10) are (using an abbreviated notation)

$$\int\int \gamma_0(Z')\mathcal{R}_0(Z,Z')\gamma_2(Z) - \gamma_0(Z')\mathcal{R}_1(Z,Z')\gamma_1(Z) + \gamma_0(Z')\mathcal{R}_2(Z,Z')\gamma_0(Z) = 0 \tag{5.11}$$

and

$$\int\int \gamma_1(Z')\mathcal{R}_0(Z,Z')\gamma_1(Z) + \gamma_1(Z')\mathcal{R}_1(Z,Z')\gamma_0(Z) = 0. \tag{5.12}$$

The results above are deduced from (5.6)–(5.8) using the symmetry $\mathcal{R}_n(Z,Z') = \mathcal{R}_n(Z',Z)$. An extra simplification comes in the case of the triangle, where we can show that for the final term in (5.10)

$$\int_0^B\int_0^B \gamma_0(Z')\mathcal{R}_2(Z,Z')\gamma_0(Z)\,dZ\,dZ' = 0. \tag{5.13}$$

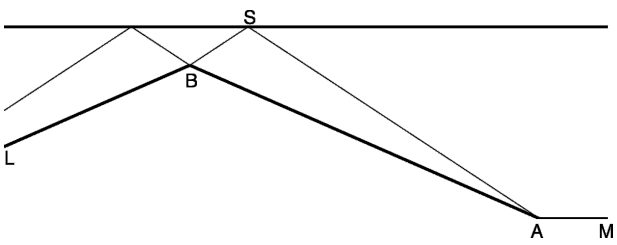

FIG. 10. The geometric construction above gives the condition (4.4) that determines the first null curve in the (A, B) plane. The bottom is LBAM.

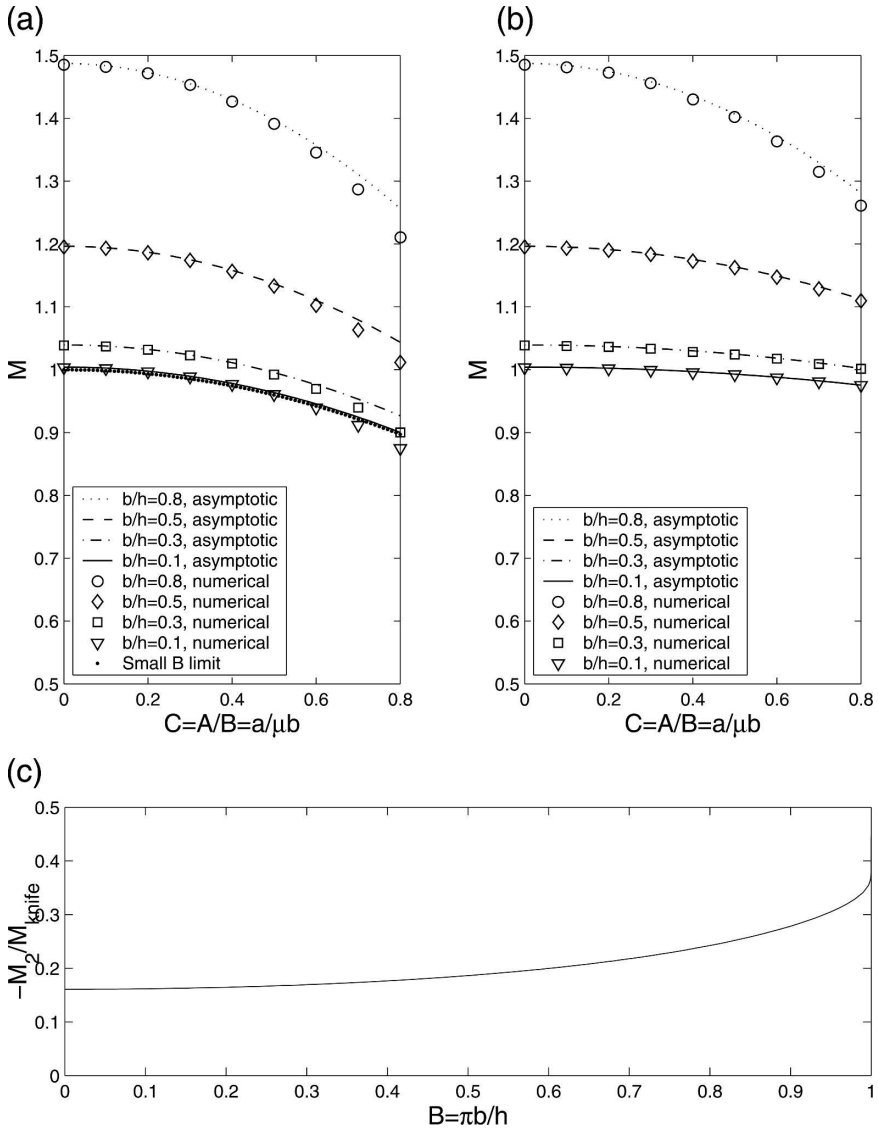

FIG. 11. (top left) Function M for the triangular ridge with $b/h = 0.8, 0.5, 0.3$, and 0.1 plotted as a function of C. Symbols: numerical results. Curves: small-C approximation (5.1). Lower dots: limit $b \ll h$. (top right) Results for the polynomial ridge. (bottom) Curvature $-M_2/M_{\text{knife}}$ for the triangular ridge.

This identity above, which we first discovered numerically, can be proved by differentiating (5.6) twice with respect to Z, using also (2.26) and (5.3). For the triangle, hence, we do not need to handle the distribution $\mathcal{R}_2(Z, Z')$, which is defined only by a divergent series in (5.5). For the polynomial ridge, however, we need the full result (5.10) since the smoothness of $Q_1(Z)$ near $Z = B$ is such that the operations required to pass from (5.6) to (5.13) are not permitted.

To calculate M_2 using (5.10) we must solve (5.7) for $\gamma_1(z)$. Because of the δ function in $\mathcal{R}_1$ this integral equation for γ_1 simplifies to

$$-Q_1(Z)\sqrt{\frac{1-\cos Z}{\cos Z-\cos B}} = \int_0^B \mathcal{R}_0(Z, Z')\gamma_1(Z')\,dZ', \tag{5.14}$$

where we have used (5.9) for $\gamma_0(z)$. After specifying a topographic profile via $Q_1(Z)$, (5.14) must usually be solved numerically. As an example, Fig. 11 compares $M(B, C)$ calculated from the two-term expansion based on (5.10) and (5.14) (curves) with the numerical solution of the complete integral equation in (2.24) (symbols). The agreement is very good. The final panel in

Fig. 11 shows the behavior of the curvature $-M_2/M_{\text{knife}}$ as a function of B.

Isolated analytic results based on solving (5.14) are possible. For example, using the triangular profile, $Q_1(Z) = B - Z$, with $B \ll 1$, we managed to obtain $\gamma_1(Z)$ and M_2. The final result is

$$M_2 = -\frac{1}{3}\left[1 + \frac{24}{\pi^2}\ln 2(\ln 2 - 1)\right] = -0.1609. \tag{5.15}$$

This is the small-B limit of the curve in the top left-hand panel of Fig. 11.

6. Conclusions

We have calculated the conversion due to a submarine ridge, concentrating on two topographic profiles: the triangular ridge and the polynomial ridge. Our results agree in the limit of a narrow ridge with those of St. Laurent et al. (2003) and Llewellyn Smith and Young (2003) for the knife-edge barrier. In the limit of gentle slopes and low barriers we recover the WTA results. From Figs. 5 and 7, we conclude that one can obtain a good rough estimate of the tidal conversion by using the knife-edge result for a supercritical ridge and the WTA result if the ridge is subcritical. In other words, these analytic cases apply to broad and complementary regions of the (A, B) parameter space. Many open questions remain, of which probably the most compelling is the effect of three-dimensionality.

Another issue concerns the physical processes that heal the singularities and inversions evident in the buoyancy field shown in Figs. 1, 6, and 8. The small-scale features and density inversions within, and close to, the internal tidal beams are not an artifact of the hydrostatic approximation: the nonhydrostatic (but subcritical) solutions of Balmforth et al. (2002) show that this singularity develops as the critical slope condition is approached. And Robinson (1969) showed that the buoyancy perturbation diverges like $|\xi|^{-1/2}$, where ξ is the normal distance from the tidal beam. Because the linear theory predicts that the disturbance diverges within the beams, the density field inevitably becomes inverted close to the singularity even if the incident velocity, U in (1.1), is very small. This singularity of linear, inviscid, and nondiffusive theory indicates missing physics and leads one to wonder if our estimates of the conversion rate are compromised.

There are several reasons for optimism. First, Robinson (1969) gave a local analysis of these beams and showed that there is no flux of mass, momentum, or energy into the singularity. In this sense tidal beams are "less singular" than, for instance, hydraulic jumps (i.e., there is a flux of energy into a hydraulic jump). Second, we have shown that the first few vertical modes contain a large fraction of the converted energy (see Fig. 9). Thus, small-scale mixing, localized within the beams, may not affect the energy-containing modes. Di Lorenzo et al. (2006) have compared the analytic formulas in this paper with energy conversion obtained using a nonlinear primitive equation ocean model. They find satisfactory quantitative agreement between the numerical model and the theory presented here. Moreover, the model results are insensitive to large variations in the explicit viscosity and diffusivity. This supports the rough argument made above that dissipation can heal the tidal singularity without significantly affecting the energy carried by the first few vertical modes.

Acknowledgments. This research was partially funded by NASA Goddard Grant NAG5-12388 and by NSF Grant OCE 0220362. We thank Gary Egbert and Jonas Nycander for helpful comments.

APPENDIX A

Calculation of $\mathbf{W}_{nk}$

The most unpleasant task is calculating the matrix $\mathbf{W}_{nk}$ in (3.7)—the integrand in (3.7) is potentially singular, so midpoint or trapezoidal approaches are not recommended. After trying various alternatives we decided that the most straightforward approach is also the best: we substitute the series in (2.26) into (3.7) and exchange summation and integration. This gives

$$\mathbf{W}_{nk} = \mathbf{W}^{(1)}_{nk} + \mathbf{W}^{(2)}_{nk}, \tag{A.1}$$

where

$$\mathbf{W}^{(1)}_{nk} = \frac{1}{2\pi}\sum_{p=1}^{\infty} p^{-1}\int_{Z_{n-1}}^{Z_n} dZ \int_{Z_{k-1}}^{Z_k} \times\ dZ'\ \sin pZ \sin pZ' e^{ip(Q+Q')} \tag{A.2}$$

and

$$\mathbf{W}^{(2)}_{nk} = \frac{1}{2\pi}\sum_{p=1}^{\infty} p^{-1}\int_{Z_{n-1}}^{Z_n} dZ \int_{Z_{k-1}}^{Z_k} \times dZ'\ \sin pZ \sin pZ' e^{ip|Q-Q'|}. \tag{A.3}$$

The matrix $\mathbf{W}^{(1)}_{nk}$ factors neatly into

$$\mathbf{W}^{(1)}_{nk} = \frac{1}{2\pi}\sum_{p=1}^{\infty} p^{-1} e^{ip(\tilde{Q}_k + \tilde{Q}_n)} U_n(p) U_k(p), \tag{A.4}$$

where $\tilde{Q}_k$ is defined in (3.3) and

$$U_n(p) \equiv \int_{Z_{n-1}}^{Z_n} \sin pZ e^{-ipS_nZ}\, dZ, = \frac{1}{ip}\left\{ \frac{e^{ip(1-S_n)\tilde{Z}_n}}{1-S_n} \sin\left[\frac{1}{2}p\Delta_n(1-S_n)\right] - \frac{e^{-ip(1+S_n)\tilde{Z}_n}}{1+S_n} \sin\left[\frac{1}{2}p\Delta_n(1+S_n)\right]\right\}. \tag{A.5}$$

If $n \neq k$ we can also factor $\mathbf{W}^{(2)}_{nk}$. Suppose $n > k$, so that $Z > Z'$ and $|Q - Q'| = Q' - Q$. [We assume that $Q(Z)$ decreases monotonically with increasing Z, from $Q(0) = A$ to $Q(B) = 0$.] Then

$$\mathbf{W}^{(2)}_{nk} = \frac{1}{2\pi}\sum_{p=1}^{\infty} p^{-1} e^{ip(\tilde{Q}_k - \tilde{Q}_n)} U^*_n(p) U_k(p), \quad \text{if} \quad n > k. \tag{A.6}$$

To get the terms with $n < k$ we use the symmetry $\mathbf{W}^{(2)}_{nk} = \mathbf{W}^{(2)}_{kn}$. Next, consider the diagonal terms, $\mathbf{W}^{(2)}_{nn}$:

$$\mathbf{W}^{(2)}_{nn} = \frac{1}{2\pi}\sum_{p=1}^{\infty} p^{-1} J_p(n, S_n), \tag{A.7}$$

where

$$J_p(n) \equiv \int_{Z_{n-1}}^{Z_n} dZ \int_{Z_{n-1}}^{Z_n} dZ' \sin pZ \sin pZ' e^{ipS_n|Z-Z'|}. \tag{A.8}$$

After some calculation

$$J_p(n) = \frac{1}{4}\Delta_n^2[K_p(n) - L_p(n)], \tag{A.9}$$

where

$$K_p(n) \equiv \int_0^2 (2-\tau)\cos\beta\tau e^{i\beta S_n\tau}\, d\tau, = \frac{\left[S_n^2 + 1 + 2i\beta S_n(S_n^2 - 1) - \frac{1}{2}(S_n - 1)^2 e^{2i\beta(S_n+1)} - \frac{1}{2}(S_n+1)^2 e^{2i\beta(S_n-1)}\right]}{\beta^2(S_n^2-1)^2}$$

and

$$L_p(n) \equiv 2\cos(2p\overline{Z}_n)\int_0^2 d\tau e^{i\beta S_n\tau}\int_0^{1-\tau/2} d\sigma \cos2\beta\sigma, = \cos(2p\overline{Z}_n)\frac{\cos2\beta + iS_n\sin2\beta - e^{2i\beta S_n}}{\beta^2(S_n^2-1)}.$$

In the above, $\beta \equiv p\Delta_n/2$.

APPENDIX B

A Nearly Critical Triangular Ridge

In this appendix we outline the calculation that leads to the point $(C, M) = (1, 16/27)$, indicated by o in Fig. 5. We need Robinson's (1969) result that the sum of the series in (2.21) is

$$\mathcal{G}(x - x', z, z') - \frac{1}{4\pi}\ln\triangleright\triangleleft, \tag{B.1}$$

where

$$\triangleright\triangleleft(X - X', Z, Z') \equiv \frac{\sin\left(\frac{|X-X'| + Z + Z'}{2}\right)\sin\left(\frac{|X-X'| - Z - Z'}{2}\right)}{\sin\left(\frac{|X-X'| + Z - Z'}{2}\right)\sin\left(\frac{|X-X'| - Z + Z'}{2}\right)}. \tag{B.2}$$

The argument of the logarithm might be negative, in which case one must use the branch determined by the radiation condition:

$$\mathcal{G}(x - x', z, z) = \frac{1}{4\pi}\ln|\triangleright\triangleleft| + \frac{\mathrm{i}}{4}L(\triangleright\triangleleft), \tag{B.3}$$

where the function L is equal to 0 or ±1, as in Fig. B1. Notice that $\ln(xy) \neq \ln(x) + \ln(y)$ (e.g., consider $x = y = -1$). Using (B.2) in (2.25) we have an alternative to the series representation of $\mathcal{R}$ in (2.26).

We now suppose that C is close to 1 with $C^2 = 1 + \epsilon$ and work in the limit $(\epsilon, B) \ll 1$. We take the expression for the kernel $\mathcal{R}$ based on (B.2) and make some simplifications, for example, expanding the various sines in the Taylor series. After some working the resulting reduction of the integral equation in (2.24) is

$$8\pi\zeta = \int_0^1 \gamma(\zeta')\left\{\ln\left[\frac{1-\zeta-\zeta'}{(1-\zeta)(1-\zeta')}\right] + \ln\left[-\frac{4\zeta\zeta'}{\epsilon(\zeta-\zeta')^2}\right]\right\} d\zeta', \tag{B.4}$$

where $\zeta \equiv z/b = Z/B$. Recalling the branch of the logarithm in (B.3), this integral equation becomes

$$8\pi\zeta = \int_0^1 \gamma(\zeta')\left[\ln\left|\frac{1-\zeta-\zeta'}{(1-\zeta)(1-\zeta')}\right| + \ln\left|\frac{4\zeta\zeta'}{\epsilon(\zeta-\zeta')^2}\right|\right] d\zeta' + i\pi\int_{1-\zeta}^1 \gamma(\zeta')\, d\zeta' + i\pi H(\epsilon)\int_0^1 \gamma(\zeta')\, d\zeta', \tag{B.5}$$

where $H(\epsilon)$ is the step function. Differentiating with respect to ζ and rearranging,

$$8\pi = \frac{1}{\zeta(1-\zeta)}\int_0^1 \gamma(\zeta')\, d\zeta' - \int_0^1 \left(\frac{1}{1-\zeta-\zeta'} + \frac{2}{\zeta-\zeta'}\right)\gamma(\zeta')\, d\zeta' + i\pi\gamma(1-\zeta). \tag{B.6}$$

At this point ϵ has disappeared from the problem. This suggests that $\int_0^1 \gamma(\zeta)\, d\zeta = 0$ in order for ϵ to drop out of (B.5).

We now put (B.6) into a standard form by defining $\zeta \equiv (1+y)/2$ and $\zeta' \equiv (1+t)/2$. We also define $\Gamma(t)$ by

$$\Gamma(t) = \gamma\left(\frac{1+t}{2}\right). \tag{B.7}$$

Notice that the definition above implies that

$$\gamma(1-\zeta) = \gamma\left(\frac{1-y}{2}\right) = \Gamma(-y). \tag{B.8}$$

Then (B.6) becomes

$$8\pi = \frac{2}{1-y^2}\int_{-1}^1 \Gamma(t)\, dt + \int_{-1}^1 \left(\frac{1}{y+t} + \frac{2}{t-y}\right)\Gamma(t)\, dt + i\pi\Gamma(-y). \tag{B.9}$$

Last, we let $y = -x$ so that

$$8\pi = \frac{2}{1-x^2}\int_{-1}^1 \Gamma(t)\, dt + \int_{-1}^1 \left(\frac{2}{t+x} + \frac{1}{t-x}\right)\Gamma(t)\, dt + i\pi\Gamma(x). \tag{B.10}$$

For now we assume, and this can be verified a posteriori, that the solution satisfies the two following conditions:

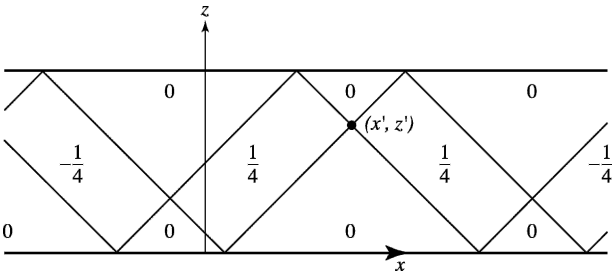

FIG. B1. The imaginary part of $\mathcal{G}(x-x', z, z')$ in (B.3) is shown above. The source is at (x', z'). This figure corrects inconsequential errors in both Fig. 1 of Robinson (1969) and in Fig. 3 of Llewellyn Smith and Young (2003).

$$\int_{-1}^1 \Gamma(t)\, dt = 0, \quad \Gamma(-x) = -\Gamma^*(x). \tag{B.11}$$

Introducing Γ_r and Γ_i, the real and imaginary part of Γ, and using (B.11) we can write (B.10) as the two coupled equations

$$\frac{8\pi}{3} = \int_{-1}^1 \frac{\Gamma_r(t)}{t-x}\, dt - \frac{\pi\Gamma_i(x)}{3} \quad \text{and}$$

$$0 = \int_{-1}^1 \frac{\Gamma_i(t)}{t-x}\, dt - \pi\Gamma_r(x). \tag{B.12}$$

We introduce $S_\pm(t) = \Gamma_r(t) \pm \Gamma_i(t)/\sqrt{3}$, which satisfies

$$\frac{8\pi}{3} = \int_{-1}^1 \frac{S_\pm(t)}{t-x}\, dt \mp \frac{\pi S_\pm(x)}{\sqrt{3}}. \tag{B.13}$$

These two equations can be transformed into a Riemann problem and solved analytically (Pipkin 1991), giving

$$S_\pm(x) = \frac{4\left(x \mp \frac{1}{3}\right)}{\sqrt{3}(1-x^2)^{1/3}(1\mp x)^{1/3}}. \tag{B.14}$$

The solution of (B.10) is hence

$$\Gamma(x) = \frac{4}{\sqrt{3}(1-x^2)^{1/3}} \times \left[e^{i\pi/3}\frac{x-\frac{1}{3}}{(1-x)^{1/3}} + e^{-i\pi/3}\frac{x+\frac{1}{3}}{(1+x)^{1/3}}\right]. \tag{B.15}$$

We can now compute the conversion. The simplest approach is to use the expression (2.34) in the small-B limit. Then

$$M = \frac{2}{\pi}\int_0^1 \Gamma_r(\zeta)\zeta\, d\zeta = \frac{1}{\pi\sqrt{3}}\int_{-1}^{1}\left[\left(\frac{1+x}{1-x}\right)^{2/3}\left(x-\frac{1}{3}\right) + \left(\frac{1+x}{1-x}\right)^{1/3}\left(x+\frac{1}{3}\right)\right] dx\,. \tag{B.16}$$

This gives $M = 16/27 \approx 0.593$. This is the point o in the upper panel of Fig. 5 that falls slightly below the numerical curves. For convergence near $C = 1$ the numerical formulation requires many terms in the series (A.4) and (A.7), and thus there is some uncertainty in the Fig. 5 curves near $C = 1$. The proximity of o to these curves is therefore reassuring. The numerical curves, and the calculation in this appendix, suggest that M is continuous at $C = 1$, but that $dM/dC \to \infty$ as $C \to 1$ from below.

REFERENCES

Althaus, A. M., E. Kunze, and T. B. Sanford, 2003: Internal tide radiation from the Mendocino Escarpment. *J. Phys. Oceanogr.,* **33,** 1501–1527.

Baines, P. G., 1973: The generation of internal tides by flat-bump topography. *Deep-Sea Res.,* **20,** 179–205.

——, 1982: On internal tide generation models. *Deep-Sea Res.,* **29,** 307–382.

Balmforth, N. J., G. R. Ierley, and W. R. Young, 2002: Tidal conversion by subcritical topography. *J. Phys. Oceanogr.,* **32,** 2900–2914.

Bell, T. H., 1975a: Lee waves in stratified fluid with simple harmonic time dependence. *J. Fluid Mech.,* **67,** 705–722.

——, 1975b: Topographically generated internal waves in the open ocean. *J. Geophys. Res.,* **80,** 320–327.

Cummins, P. F., J. Y. Cherniawsky, and M. G. G. Foreman, 2001: North Pacific internal tides from the Aleutian Ridge: Altimeter observations and modeling. *J. Mar. Res.,* **59,** 167–191.

Di Lorenzo, E., W. R. Young, and S. G. Llewellyn Smith, 2006: Numerical and analytical estimates of M_2 tidal conversion at steep oceanic ridges. *J. Phys. Oceanogr.*, **36,** 1072–1084.

Egbert, G. D., and R. D. Ray, 2001: Estimates of M_2 tidal energy dissipation from TOPEX/Poseidon altimeter data. *J. Geophys. Res.,* **106,** 22 475–22 502.

Kang, S. K., M. G. G. Foreman, W. R. Crawford, and J. Y. Cherniawsky, 2000: Numerical modeling of internal tide generation along the Hawaiian Ridge. *J. Phys. Oceanogr.,* **30,** 1083–1098.

Khatiwala, S., 2003: Generation of internal tides in the ocean. *Deep-Sea Res. I,* **50,** 3–21.

Ledwell, J. R., E. T. Montgomery, K. L. Polzin, L. C. St. Laurent, R. W. Schmitt, and J. M. Toole, 2000: Evidence of enhanced mixing over rough topography in the abyssal ocean. *Nature,* **403,** 179–182.

Llewellyn Smith, S. G., and W. R. Young, 2002: Conversion of the barotropic tide. *J. Phys. Oceanogr.,* **32,** 1554–1566.

——, and ——, 2003: Tidal conversion at a very steep ridge. *J. Fluid Mech.,* **495,** 171–191.

Merrifield, M. A., and P. E. Holloway, 2002: Model estimates of M_2 internal tide energetics at the Hawaiian Ridge. *J. Geophys. Res.,* **107,** 3179, doi:10.1029/2001JC000996.

——, ——, and T. M. S. Johnston, 2001: The generation of internal tides at the Hawaiian Ridge. *Geophys. Res. Lett.,* **28,** 559–562.

Munk, W. H., and C. I. Wunsch, 1998: Abyssal recipes II: Energetics of tidal and wind mixing. *Deep-Sea Res.,* **45,** 1977–2010.

Pipkin, A. C., 1991. *A Course on Integral Equations.* Springer Verlag, 268 + xiii pp.

Ray, R. D., and G. T. Mitchum, 1996: Surface manifestation of internal tides generated near Hawaii. *Geophys. Res. Lett.,* **23,** 2101–2104.

Robinson, R. M., 1969: The effects of a barrier on internal waves. *Deep-Sea Res.,* **16,** 421–429.

Rudnick, D. L., and Coauthors, 2003: From tides to mixing along the Hawaiian Ridge. *Science,* **301,** 355–357.

St. Laurent, L., and C. J. R. Garrett, 2002: The role of internal tides in mixing the deep ocean. *J. Phys. Oceanogr.,* **32,** 2882–2899.

——, S. Stringer, C. J. R. Garrett, and D. Perrault-Joncas, 2003: The generation of internal tides at abrupt topography. *Deep-Sea Res. I,* **50,** 987–1003.